Exp Fluids (2009) 46:165–179
DOI 10.1007/s00348-008-0551-z

RESEARCH ARTICLE

In-cylinder tumble flows and performance of a motorcycle engine with circular and elliptic intake ports

**R. F. Huang · K. H. Lin · C.-N. Yeh ·
J. Lan**

Received: 28 October 2007 / Revised: 14 June 2008 / Accepted: 4 August 2008 / Published online: 25 August 2008

Abstract The temporal and spatial evolution processes of the flows in the cylinder of a four-valve, four-stroke, single cylinder, reciprocating motorcycle engine installed with the elliptic and circular intake ports were experimentally studied by using the particle image velocimetry (PIV). The engine was modified to fit the requirements of PIV measurement. The velocity fields measured by the PIV were analyzed and quantitatively presented as the tumble ratio and turbulence intensity. In the symmetry plane, both the circular and elliptic intake ports could initiate a vortex around the central region during the intake stroke. During the compression stroke, the central vortex created in the cylinder of the engine with the circular intake port disappeared, while that in the engine cylinder with the elliptic intake port further developed into the tumble motion. In the offset plane, weak vortical structures were initiated by the bluff-body effect of the intake valves during the intake stroke. The vortical structures induced by the elliptic intake port were more coherent than those generated by the circular intake port; besides, this feature extends to the compression stroke. The cycle-averaged tumble ratio and the turbulence intensity of the engine with the elliptic intake port were dramatically larger than those of the engine with the circular intake port. The measured engine performance was improved a lot by installing the elliptic intake port. The correlation between the flow features and the enhancement of the engine performance were argued and discussed.

List of symbols

A/F	air/fuel ratio
BSFC	break specific fuel consumption (=fuel consumption rate divided by output power of engine) (g/PS h)
CA	crank angle (°)
C_{HC}	concentration of hydrocarbon emission (ppm)
I	turbulence intensity at each grid point at a certain crank angle (=root-mean-square values of fluctuation velocities divided by average engine speed)
I_{CA}	plane-averaged turbulence intensity at a certain crank angle (=arithmetic average of I)
$\bar{I}$	cycle-averaged turbulence intensity (=arithmetic average of I_{CA} over intake and compression strokes)
L	lift of valve (mm)
N	engine speed (rpm)
n	number of grid points
T	torque of engine output (kg m)
$T_{v,\ \mathrm{CA}}$	plane-averaged tumble ratio of in-cylinder flow defined by Eq. 1
$\overline{T_v}$	cycle-averaged tumble ratio (=arithmetic average of $T_{v,\ \mathrm{CA}}$ over intake and compression strokes)

R. F. Huang (✉) · K. H. Lin
Department of Mechanical Engineering,
National Taiwan University of Science and Technology,
Taipei 10672, Taiwan, ROC
e-mail: rfhuang@mail.ntust.edu.tw

C.-N. Yeh
R & D Center, Sangyang Industry Co.,
Hsin Fong Shiang, Hsinchu County, Taiwan, ROC
e-mail: 27342@sym.com.tw

J. Lan
Department of Power Vehicle and Systems Engineering,
National Defense University, Tai-His,
Tao-Yuan 33509, Taiwan, ROC
e-mail: lanjen@ccit.edu.tw

P	power of engine output (PS)
R	radius of engine cylinder bore (=26.2 mm)
X	horizontal coordinate originated at left cylinder wall
Y	vertical coordinate originated at lower-left corner of cylinder when piston at bottom dead center
α	throttle valve opening (proportion of opening out of full opening)
υ	kinematic viscosity of air (m^2/s)
ω	crank shaft angular speed (radians per second)

1 Introduction

The in-cylinder flow is a decisive factor for combustion in the internal combustion engine, which in turn provides significant effects on the engine performance (Heywood 1988). Turbulence intensity is one of the key parameters which can lead to high engine performance and low emission (Heywood 1987). The higher turbulence is believed to generate both faster flame-front propagation and higher reactive flame-surface area. There are a number of ways to enhance the turbulence intensity in the cylinder of a reciprocating engine. Generating a significant vortical flow motion (tumble and/or swirl) inside the engine cylinder during the intake process is one of the more promising methods to achieve fast burning rate because a well defined single vortical structure is stabler than other large scale in-cylinder flows. Therefore, it may break up later in the cycle to give higher turbulence during combustion (Rask 1979).

Understanding of the evolution process of fluid motion in internal combustion engines therefore is critical for the engine designs to develop the most attractive operating and emission characteristics. Some investigators have conducted diagnosis of the in-cylinder flow of the reciprocating engines by using the laser Doppler velocimeter (Rask 1979; Ekchian and Hoult 1979; Arcoumanis et al. 1998) or the particle image velocimeter (Khalighi 1991; Reeves et al. 1999; Calendini et al. 2000; Huang et al. 2005; Stansfield et al. 2007). Some results suggested that large turbulence intensities were primarily induced by the shear effects of the inducted jet and the vortical flow motions which were evolved during the engine cycles. Stansfield et al. (2007) showed that the flow patterns of the in-cylinder flow would look “similar” at low and high engine speeds. In their study, the typical flow pattern in the symmetry plane of the engine cylinder during the mid-intake stroke period was: one counterclockwise-rotating vortex appeared around the corner near the inlet valves, one clockwise-rotating vortex presented around the corner opposite to the inlet-valve corner, and the cross-cylinder flow was induced in the region between these two corner vortices. It was found that at high engine speed the vortex sizes at corners were enlarged and therefore led to higher tumble ratio. However, the detailed evolution process of the vortical flow structure and its influences on the engine performance were still unclear.

As indicated by investigators (Heywood 1987, 1988), the temporal and spatial evolution processes of the in-cylinder flow structure depend enormously on the intake port/valve configuration, chamber geometry, piston shape, squish area, and probably connecting rod. Two intake-port configurations (circular and elliptic) were employed in this study in order to understand the formation process of the tumble vortex in the engine cylinder and its effects both on the statistic flow characteristics and the engine performance. The influences of the intake port configuration on the flow features were also discussed.

2 Experimental configuration

2.1 Apparatus

A four-stroke, four-valve, single-cylinder, motorcycle engine, was used for the study. Some important geometric and operating parameters of the engine were listed in Table 1. The shape of the cylinder head was hemispherical on the top of the combustion chamber. The configurations of ports and cylinder head of the engine were shown in the subsets of Fig. 1.

In order to perform PIV measurements, the original metallic cylinder was replaced by a transparent cylinder which was made of a customized material (mixture of 95% acrylic and 5% glass) so that the cylinder wall could resist material creep and surface crazing under the experimental conditions of this study, as shown in Fig. 1. The thickness of the transparent cylinder was 5 mm. The piston was modified so that the laser-light sheet and view angle of the camera would not be interfered by the original engine configuration.

Table 1 Important geometric parameters of engine for experiments

Bore	52.4 mm
Stroke	57.8 mm
Displacement	124.6 cm^3
Compression ratio	10.5:1
Diameter of inlet valves	19.7 mm
Diameter of exhaust valves	17.0 mm
Lift of inlet valves	6.8 mm
Lift of exhaust valves	6.6 mm
Crank angles for close/open of inlet valves	80° bTDC/106° aBDC
Crank angles for close/open of exhaust valves	94° bBDC/72° aTDC

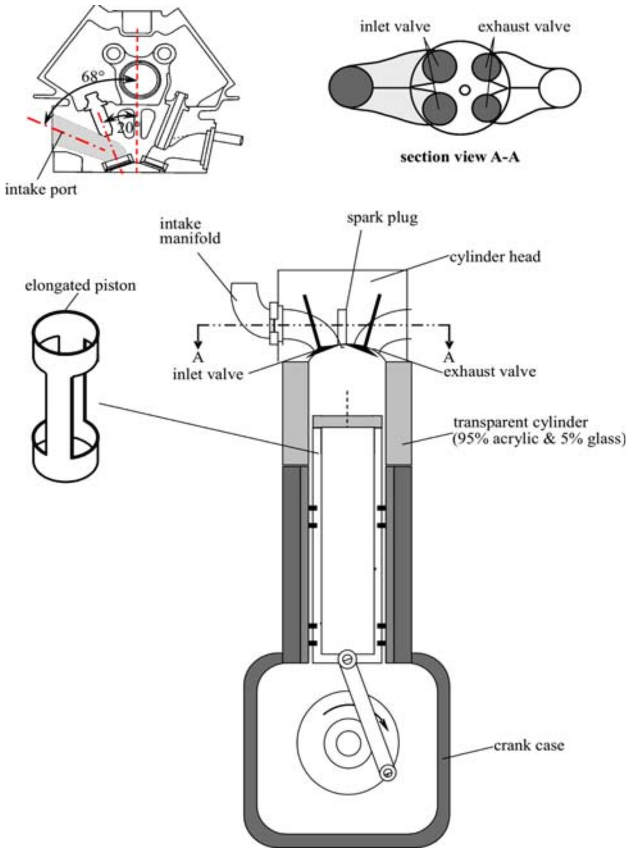

Fig. 1 Modified engine for PIV measurements

Anti-reflection black paints were spray-coated on some regions of the inner-wall of the cylinder to avoid reflection and flare of laser light. Four piston rings were inserted between the elongated piston and the cylinder at specially arranged locations to reduce the blow-by of air and the slapping of elongated piston. The locations of piston rings were set around the mid and lower sections so that they would not run on the transparent cylinder. With this arrangement, the crevice volume of the modified engine was slightly increased by about 0.02% (0.024 cm^3) when compared with the original engine, therefore the compression ratio was just slightly reduced. The measured maximum pressures of the motored unmodified and modified engines during the compression stroke were 16 and 15.7 bar, respectively.

The valve timings were shown in Fig. 2. The crank angle at the beginning of the intake stroke (the piston at top dead center, TDC) was defined as CA = 0°. The end of intake stroke (the piston at bottom dead center, BDC) was CA = 180°. The compression stroke therefore started from CA = 180° and ended at CA = 360°. The maximum lifts L of the intake and exhaust valves were 6.8 and 6.6 mm, respectively. The instantaneous crank angle was indicated by output signals of an encoder which was mounted to the crank axis. The encoder had a resolution of 1°-crank angle.

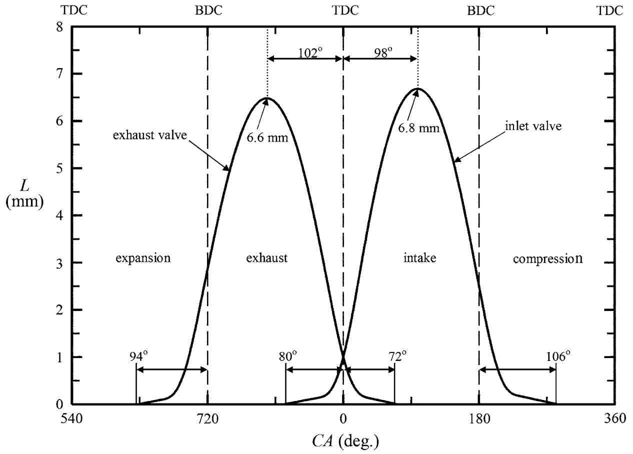

Fig. 2 Lift histories of intake and exhaust valves

The "Z" signal (one pulse per revolution) and "A" signal (360 pulses per revolution) of the encoder outputs were used to indicate the BDC and crank angles, respectively, and also served as signals to trigger the electronic synchronizers of PIV.

Two intake ports with different shapes at the entrances of the ports, as shown in Fig. 3, were employed for experiments. One had a circular cross section with a diameter of 23 mm. The other one had a near-elliptic cross section with long and short axis of 25.8 and 20.4 mm, respectively. The areas of the circular and elliptic cross sections were 415 and 413 mm^2, respectively. The near-elliptic cross section at the entrance retracted gradually back to circular shape in the intake port at a distance about 10 mm from the entrance. The geometries of the other portions of the two intake ports and the connecting tubes/hoses were maintained all the same.

The engine was driven by an electric motor whose rotating speed was controlled by a low-noise inverter. All measurements in this study were performed at the engine speed $N = 2{,}000$ rpm. The whole modified engine was mounted on a specially designed anti-vibration test rig. The

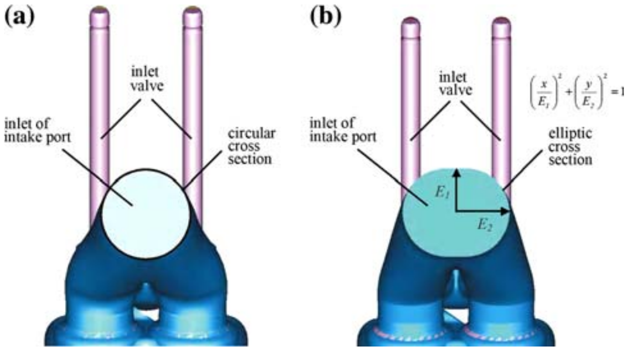

Fig. 3 Intake port configuration used for experiments. **a** Circular, **b** elliptic

maximum vibration amplitudes of the test rig at the engine speed of 2,000 rpm in the axial and lateral directions measured by a laser vibration meter were 1 and 3 μm, respectively. In terms of camera resolution which will be discussed in the following paragraphs, these vibration amplitudes corresponded to only about 0.02 and 0.06 pixels and would make very little influence on the measurement accuracy.

In order to examine the correlation between the in-cylinder flow motions and the engine performance, the real engine without modification of cylinder (refer to Table 1 for specifications) was hooked up to a test rig and connected to an eddy-current dynamometer (Model W-40, Tokyokoki-Schenck) via two rubber couplings and a homemade driveshaft. The maximum power, torque, and speed of the dynamometer were 60 PS, 7.612 kg m, and 17,000 rpm, respectively. The load cell was made by the Interface Co. (model SSN-AJ-500N). The exhaust concentrations were measured by gas analyzers (Model MEXA-554JA, Horiba Co.)

The engine performance would be hugely influenced by the volumetric efficiency (sometimes called the “air-intake efficiency”, i.e., the measured realistic intake airflow rate divided by the theoretical intake airflow rate). If the volumetric efficiency was appreciably changed by modification of the inlet-port, it would be difficult to distinguish parametric effects (in-cylinder flow or volumetric efficiency) on the engine performance. In order not to mix up the influential parameters, the volumetric efficiency was carefully examined by measuring the inlet air quantity with a calibrated hot-wire type airflow meter (Model 730Accu-Mass, Sierra Instruments). Because the open/close motions of the valves would induce oscillating flows and therefore deviate the measurement results of the hot-wire type airflow meter, a large buffer tank was incorporated into the piping system in order to reduce the effect induced by the flow oscillation.

2.2 Instrument

A particle image velocimeter (PIV) system, included a Nd:YAG laser, a CCD camera, and a home-made electronic controller, was used for the visualization of the in-cylinder flow. The electronic controller consisted of two parts: the “rotating-device signal coordinator” and the “laser double-pulse timing controller.” The “rotating-device signal coordinator” received series of TTL-compatible signals from an encoder which was mounted on the crank-shaft of the engine. Functions like “number of leading-revolutions to skip before outputting trigger signal”, “number of revolutions for outputting one trigger signal”, “crank angle for outputting one signal”, and “total number of output signals” were built-in, so that the technique of conditional sampling could be used. The TTL-compatible output signals of the “rotating-device signal coordinator” were fed to the “laser double-pulse timing controller” according to the timing settings. The “laser double-pulse timing controller” had the functions of outputting TTL signals to control the timings for flashing of the lasers and shuttering of the camera. Time separations between the triggering signals of “rotating-device signal coordinator” and the lamping, the lamping and the Q-switching, as well as the first and the second lamping were flexibly adjustable. Time separation between consecutive flashes of the lasers could be easily set between 0 and 9,999 μs at a resolution of 0.1 μs. The wavelength of the laser-light beam was 532 nm (green). The laser could operate at the double-pulse mode with the maximum pulsing rate of 15 pairs per second. The maximum pulsing energy of the laser was 90 mJ. During the experiments, the laser pulsing energy was regulated between 55 and 5% of the maximum energy. The pulse width was between 3 and 5 ns. The light beams emitted from the laser head were expanded into a 20° light sheet through a laser-light sheet generator which was installed at the exit of the laser-head. The thickness of laser-light sheet was adjusted to about 0.5 mm.

Plastic particles made of polyamide were seeded into the engine through a cyclone particle generator to scatter the laser light. The particles were introduced into the intake pipe through two mountings attached perpendicularly to the direction of the engine airflow. The throttle valve was set wide open. The particles were almost spherical when inspected under the microscope. The Sauter mean diameter was about 1.8 ± 0.8 mm when measured by the Malvern 2600C Particle Analyzer. The density was 1,008 kg/m^3 at 25°C. The cut-off frequency in the turbulent flow estimated according to Mei’s method (Mei 1996) was about 1 kHz.

The particle images were recorded by Charged Coupled Device (CCD) camera which offered a maximum framing rate of 30 frames per second. The resolution was 1,008 × 1,018 pixels. When focused onto the symmetry plane, the pixel array was zoomed and mapped to a physical region of 46 × 46 mm^2 (as shown in Fig. 4) so that the spatial resolution was about 46 μm/pixel. The size of the view-window of the offset plane was 43 × 43 mm^2. The target planes were illuminated by the laser-light sheet, and the camera was arranged to face the plane at a 90° angle. A “triggered double exposure mode” (frame straddling technique) facilitated the application of particle image velocimeter. When operated at the double exposure mode, the maximum framing rate turned out to be 15 pairs per second. In this study, the image pairs were taken every four engine revolutions so that the average framing rate was around 8.3 pairs per second when the engine was motored at 2,000 rpm. Totally, 500 image pairs were taken and stored in the computer memory for each run of experiment. Various separation times between

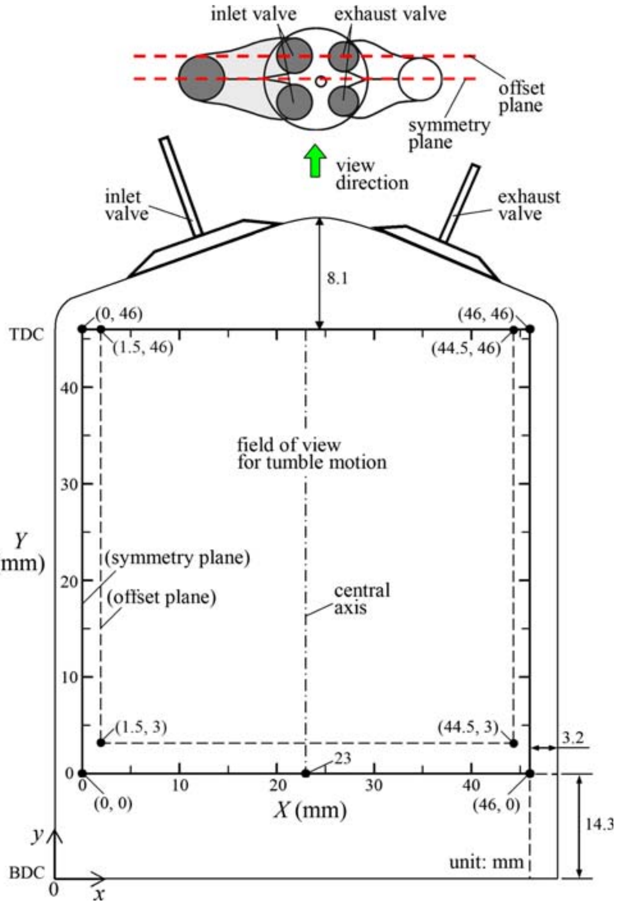

Fig. 4 Image planes (symmetry and offset planes) and coordinate system for detection of tumble motion

the consecutive laser pulses were evaluated. Finally, 20 µs was optimized for this study.

Two consecutive image frames were analyzed by using the cross-correlation technique (Keane and Adrian 1992) which was imbedded in the PIV analysis software. Because the particle images would experience the optical aberrations in radial direction caused by the curved cylinder wall, an image calibration was first applied to correct the aberrations by inserting a precision rule into the transparent cylinder at the target plane and photographed by a high-resolution digital camera. A second precision rule was simultaneously placed outside the cylinder and photographed for reference and comparison. Both the symmetry and offset planes were calibrated. For instance, the calibration curves for the symmetry plane were approximated by

$$\frac{r_{\mathrm{cor}}}{R} = 1.0047 \times \frac{r_{\mathrm{def}}}{R} \quad \text{for } 0 < r_{\mathrm{def}}/R \le 0.4580 \tag{1}$$

$$\frac{r_{\mathrm{cor}}}{R} = 0.2107 \times \left(\frac{r_{\mathrm{def}}}{R}\right)^2 + 0.7903 \times \left(\frac{r_{\mathrm{def}}}{R}\right) + 0.0540 \quad \text{for } r_{\mathrm{def}}/R \ge 0.4580 \tag{2}$$

where the symbols r_{def} and r_{cor} denoted the deflected and corrected radial coordinates, respectively. It is apparent that the aberration is less appreciable around the central region (e.g., at $r_{\mathrm{def}}/R = 0.8778$ the deviation is less than 0.5%). It becomes significant near the cylinder wall. For instance, the deviation is about 3.5% at the edge of the view window (i.e., $r_{\mathrm{def}}/R = 0.87786$). The interrogation window was set to 32 × 32 pixels. The number of vectors (the grids) predetermined for the PIV analysis results was set to 12,600. Error check and interpolation were used to identify outliers and then regenerate interpolated values to replace the identified outliers. In general, less than 2% of spurious vectors per instantaneous field were detected and replaced by the interpolation values in this study.

2.3 Uncertainties

The uncertainty estimates for each variable in the graphs were based on the method of Abernethy et al. (1985) The total uncertainty E of the variables could be found by combing systematic and random errors as $E = [F^2 + (aS_{\mathrm{D}})^2]^{1/2}$, where F is the systematic uncertainty, S_{D} the SD of the mean, and the degree of freedom a is determined as 2 for a 95 confidence level. The systematic uncertainty F was estimated according to the calibration data and previous test experience, and the SD of the mean S_{D} was computed from the raw measurement data. The uncertainties of the velocity and velocity fluctuation measurements were estimated to be about ±2.25 and ±3.41%, respectively, of the measured values.

3 Results and discussion

3.1 Evolution of tumble flow motion

The engine shows a high level of cycle-to-cycle variation, examples of which are shown in Fig. 5a–c for CA = 120°. The instantaneous velocity vector maps shown in these figures present irregular and highly turbulent flow patterns. As such, mean vector fields need to be ensemble-averaged for each fixed instant (or crank angle). It is found that the ensemble average obtained by using more than 40 data maps is enough to yield almost identical flow patterns and velocity vectors. For comparison, 46 data maps were enough to obtain stable ensemble average in Stansfield et al.'s study (2007). Figure 5d shows the ensemble average of 100 instantaneous velocity vector maps for CA = 120° in the symmetry plane. All the velocity vectors presented in Figs. 6, 7, 8 and 9 are obtained by using 500 instantaneous data maps measured by the PIV. The in-cylinder flow is actually complex and three dimensional. Two-dimensional stream-line representation would not be

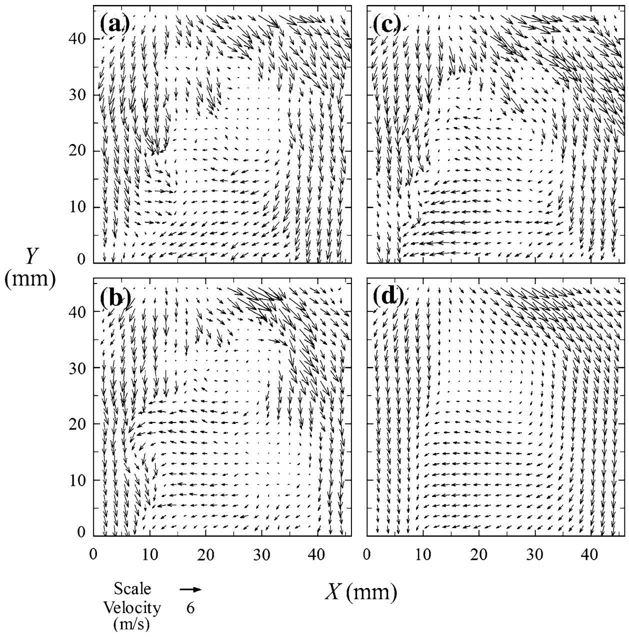

Fig. 5 Typical velocity vector maps in symmetry plane of engine with circular intake port. CA = 120°. **a–c** instantaneous vectors obtained at different cycles, **d** ensemble-average over 100 cycles

suitable for description of the flow field. However, partly because the swirl components in this study (which are not shown here) are comparatively small, and also partly because the topological flow patterns are more convenient to be analyzed by inspecting the two-dimensional streamlines, the streamlines obtained by using the stream-function method (Yuan 1967) are superimposed onto the velocity vector maps in Figs. 6, 7, 8 and 9 for identification of flow features.

3.1.1 *Flows in symmetry plane*

Figure 6 shows the evolution process of flow structure in the symmetry plane of the engine cylinder during the intake and compression strokes when the circular intake port is installed. As the inlet valves open, the air is drawn into the cylinder due to the downward motion of the piston. When the flows divert around the inlet valves, two neighboring parallel "annular jets" would be formed (Huang and Tsai 2001). The two neighboring annular jets merge at the symmetry plane [where no "bluff-body" (i.e., the valve) exists] to form the flow pattern of Fig. 6a. No recirculation bubble is observed. As the piston moves further downward, some topological flow features (Hunt et al. 1978) appear. A "positive open bifurcation line" (where the streamlines branch out of the bifurcation line) and a "negative open bifurcation line" (where the streamlines branch into the bifurcation line) are shown in Fig. 6b and c. The "positive open bifurcation line" is formed because the lateral components (in $+Z$ and $-Z$ directions) of the two annular jets impinge at the symmetry plane ($Z = 0$). The air streams in the right side of the "positive open bifurcation line" impinge the right cylinder wall, flush downward, turn leftward, and therefore make the "positive open bifurcation line" curves leftwards in the lower part of the view window. Because the airflow in the left side of the "positive open bifurcation line" goes down- and rightward, it meets the flow which is going leftward and downward from the right and hence forms the "negative open bifurcation line" in the lower-left part of the view window. The streamlines in-between the positive and negative bifurcation lines look like an "inverse *S*". During the rest of the intake stroke, as shown in Fig. 6d and e, the flows in the "inverse *S*" region further develop into a clockwise-rotating vortex around the central part of the view window. This central vortex is associated with a four-way saddle point in order to satisfy the flow topology. During the compression stroke (Fig. 6f–i), the clockwise-rotating vortex does not develop into larger-scale "tumble motion". Instead, it is destroyed by the compression effect induced by the upward-moving piston, as shown in Fig. 6f, and develops into a "sink point" in-between the bifurcation lines, as shown in Fig. 6g. The upward-motion of the piston induces appreciable upward flow velocities around the piston head. These upward-moving flows impinge the downward-moving currents and form a "negative open bifurcation line" extending from the lower-right corner to the upper-left corner of the view window, as shown in Fig. 6h and i.

Figure 7 shows the evolution process of flow structure in the symmetry plane of the engine cylinder during the intake and compression strokes when the elliptic intake port is installed. During the intake stroke, the evolution process of the flow structure of the engine with the elliptic intake port behaves similarly to that with the circular intake port (compare Figs. 7a–e with 6a–e). However, the central vortex in the engine cylinder with the elliptic intake port is formed earlier than that with the circular intake port (compare Figs. 7c with 6c). Contrary to the circular intake port, during the compression stroke the central vortex of the in-cylinder flow of the engine with the elliptic intake port is not destroyed by the upward motion of the piton, as shown in Fig. 7f–i. It becomes two clockwise-rotating vortices separated by a saddle point, as shown in Fig. 7f and g. At CA = 270° (Fig. 7h), the clockwise-rotating vortices evolve into one single vortex due to the compression effect, as shown in Fig. 7h. Although this single vortex finally disappears during the final stage of the compression stroke, as shown in Fig. 7i, the flow pattern still shows tendency of rotation in clockwise sense. It is apparent that the in-cylinder flow induced by the elliptic

Fig. 6 Evolution of flow in symmetry plane during intake stroke (**a–e**) and compression stroke (**f–i**). Engine installed with circular intake port

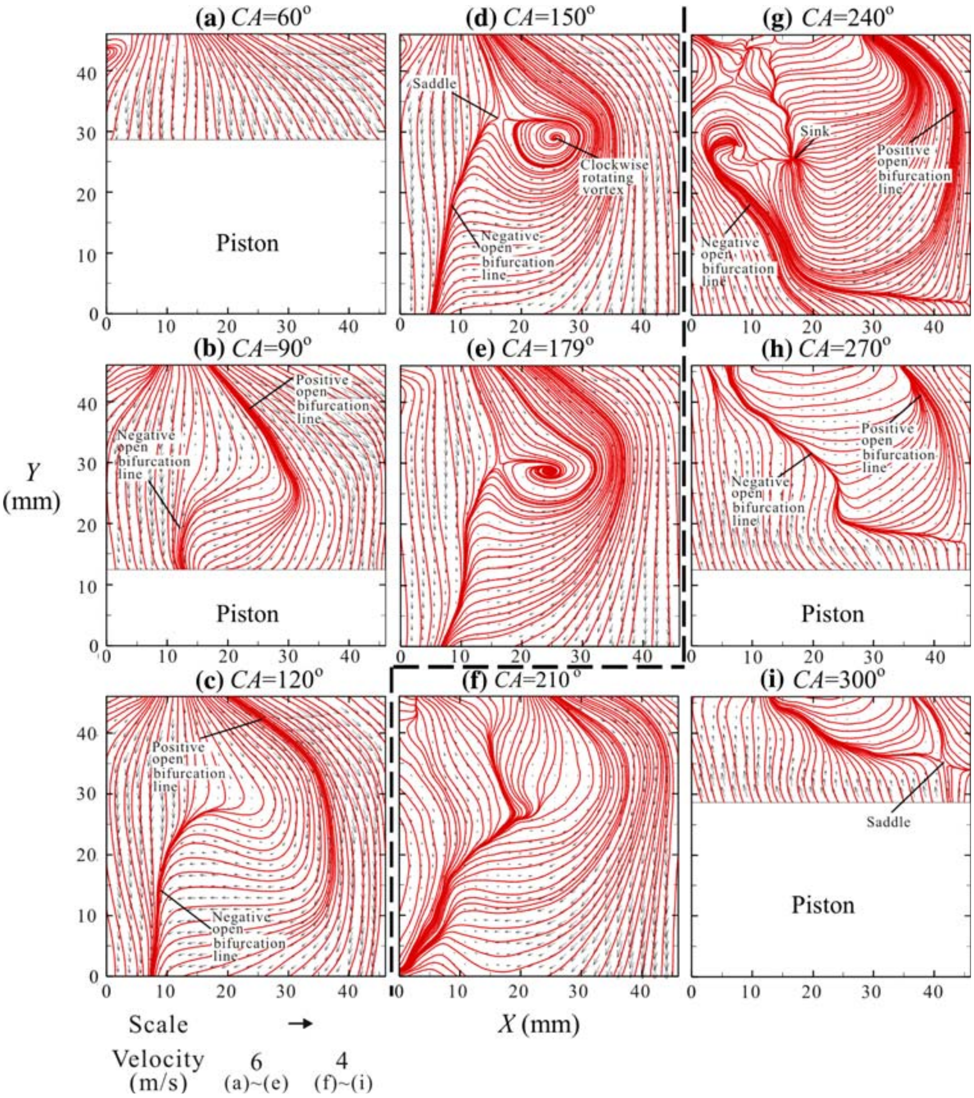

intake port presents stronger coherent characteristics of vortical flow structure than that induced by the circular intake port.

3.1.2 Flows in offset plane

The flow patterns in the offset plane present different appearances (Figs. 8, 9) from their counterparts in the symmetry plane (Figs. 6, 7). As stated previously for Fig. 4, the view-window of the offset plane cut through the center of one of the inlet valves. The inlet valve acts as a bluff body when the airflow passes over it. It is well known (e.g. Huang and Lin 1994) that when a flow passes over a bluff body, a recirculation zone would be formed in the near wake region. A "four-way saddle" would appear at the vertex of the recirculation zone. The reverse flows would be found around the central area of the recirculation zone due to the low pressure generated in the wake of the bluff body. In Figs. 8a and 9a for CA = 60°, it is not surprising that a four-way saddle is formed at a distance from the face of the inlet valve. The reverse flows going toward the valve surface can be found in-between the inlet valve and the saddle point. Downstream the saddle point, the flows go away from the inlet valve. As the piston moves further down during the intake stroke, the flows are "stretched" and the four-way saddles disappear, as shown in Figs. 8b, c and 9b, c for the circular and elliptic intake ports, respectively. During the final period of the intake stroke (Figs. 8d, e and 9d, e) for the circular and elliptic intake ports, respectively), weak vortical structures are formed. When Figs. 8d, e and 9d, e are compared, it is apparent that the vortical structures induced by the elliptic intake port are more coherent than those generated by the circular intake port. By examining and comparing the velocity vector fields and streamlines in the compression strokes as shown in Figs. 8f–i and 9f–i, it is obvious that the influences of the flow features developed

Fig. 7 Evolution of flow in symmetry plane during intake stroke (**a**–**e**) and compression stroke (**f**–**i**). Engine installed with elliptic intake port

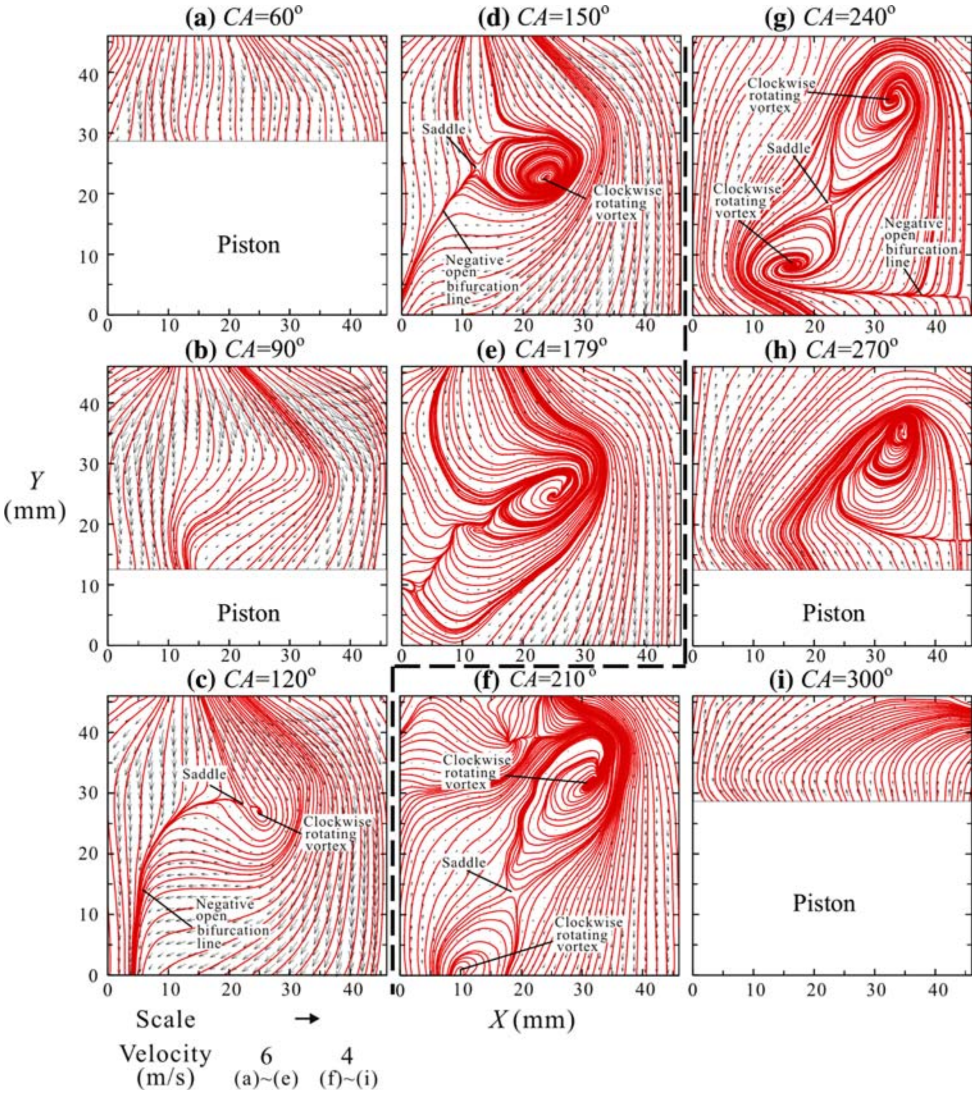

during the final periods of the intake strokes extend to the whole compression strokes: the vorticities (or roughly the tendency of rotation) induced by the elliptic intake port are larger than those induced by the circular intake port.

3.2 Turbulence intensity distributions

In order to obtain the distributions of turbulence intensity I, the mean velocity and root-mean-square value of the fluctuation velocity over 500 PIV data maps at each grid point for each crank angle are calculated. The turbulence intensity at each grid point for each crank angle is obtained subsequently by dividing the root-mean-square value of the fluctuation velocities by the mean piston speed. The turbulence intensities approach stable values as the instantaneous data used for processing are more than about 60. All the turbulence intensities presented in Figs. 10 and 11 are obtained by using 500 instantaneous data maps measured by the PIV. They are actually a statistical quantity of “temporal variation” related to cycle-to-cycle variation and turbulence. It is a measure of the extent of deviation from the mean because the mean square value of the fluctuations is the “variance” in statistics.

The contours of the turbulence intensities I (in percentage) at various crank angles in the symmetry plane of the engine cylinder which are installed with the circular intake port are shown in Fig. 10. During the intake stroke, the turbulence intensities around the region right to the positive open bifurcation line and the region left to the negative open bifurcation line present higher values than the other regions, as shown in Fig. 10a–e. This phenomenon is induced by the large shear effect developed around these areas. During the compression stroke, higher turbulence intensities are created around the lower-left corner, as shown in Fig. 10f–i, because the in-cylinder flow is subject to the influence of the upward motion of the piston. In this case, it leads the negative open

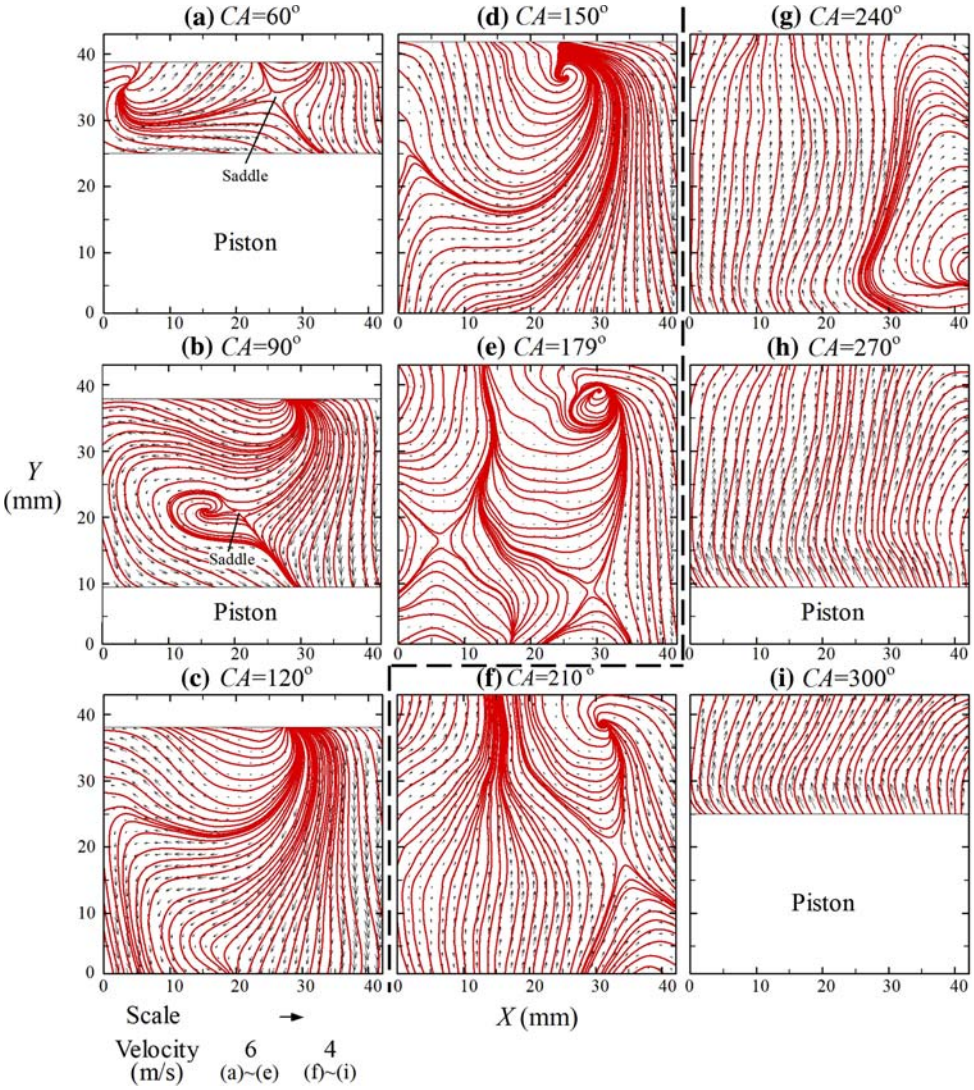

Fig. 8 Evolution of flow in offset plane during intake stroke (**a**–**e**) and compression stroke (**f**–**i**). Engine installed with circular intake port. Average taken over 500 instantaneous data maps

bifurcation line to reverse. The turbulence intensity distributions in the symmetry plane of the engine cylinder installed with the elliptic intake port are shown in Fig. 11. The features are similar to that observed in Fig. 10. However, the numerical values in the high turbulence intensity regions are generally larger than their counterparts with the circular intake port. This phenomenon is particularly apparent during the compression stroke.

3.3 Plane- and cycle-averaged tumble ratios and turbulence intensities

3.3.1 Tumble ratios

In order to quantify the above mentioned tumble flow motions, a plane-averaged tumble ratio at a certain crank angle ($T_{v,\mathrm{CA}}$) is defined as follows:

$$T_{v,\mathrm{CA}} = \frac{\sum_{i=1}^{n}\left(\frac{\partial v}{\partial X} - \frac{\partial u}{\partial Y}\right)_i}{2n\omega} \tag{3}$$

where $\left(\frac{\partial v}{\partial X} - \frac{\partial u}{\partial Y}\right)$ is the conventionally used definition of vorticity for flow. In the Eq. 3, the subscript i stands for the number of grids set up for the data points in the target plane, n is the total number of grid points, and ω the crank shaft angular speed in radians per second which can be calculated by $\omega = 2\pi N/60$ (N is the engine speed in rpm). In conducting calculations of the vorticity $\left(\frac{\partial v}{\partial X} - \frac{\partial u}{\partial Y}\right)_i$, central difference scheme is applied at each grid point. The numerator in Eq. 3 represents the total amount of large- and small-scale rotations in the target plane. For a rotating rigid body, vorticity has a constant value equal to twice the angular velocity. Therefore, the tumble ratio, $T_{v,\mathrm{CA}}$, can be interpreted as the ratio of the mean angular velocity of the vortices in the target plane at a certain crank angle normalized by the average crank speed.

Fig. 9 Evolution of flow in offset plane during intake stroke (**a**–**e**) and compression stroke (**f**–**i**). Engine installed with elliptic intake port. Average taken over 500 instantaneous data maps

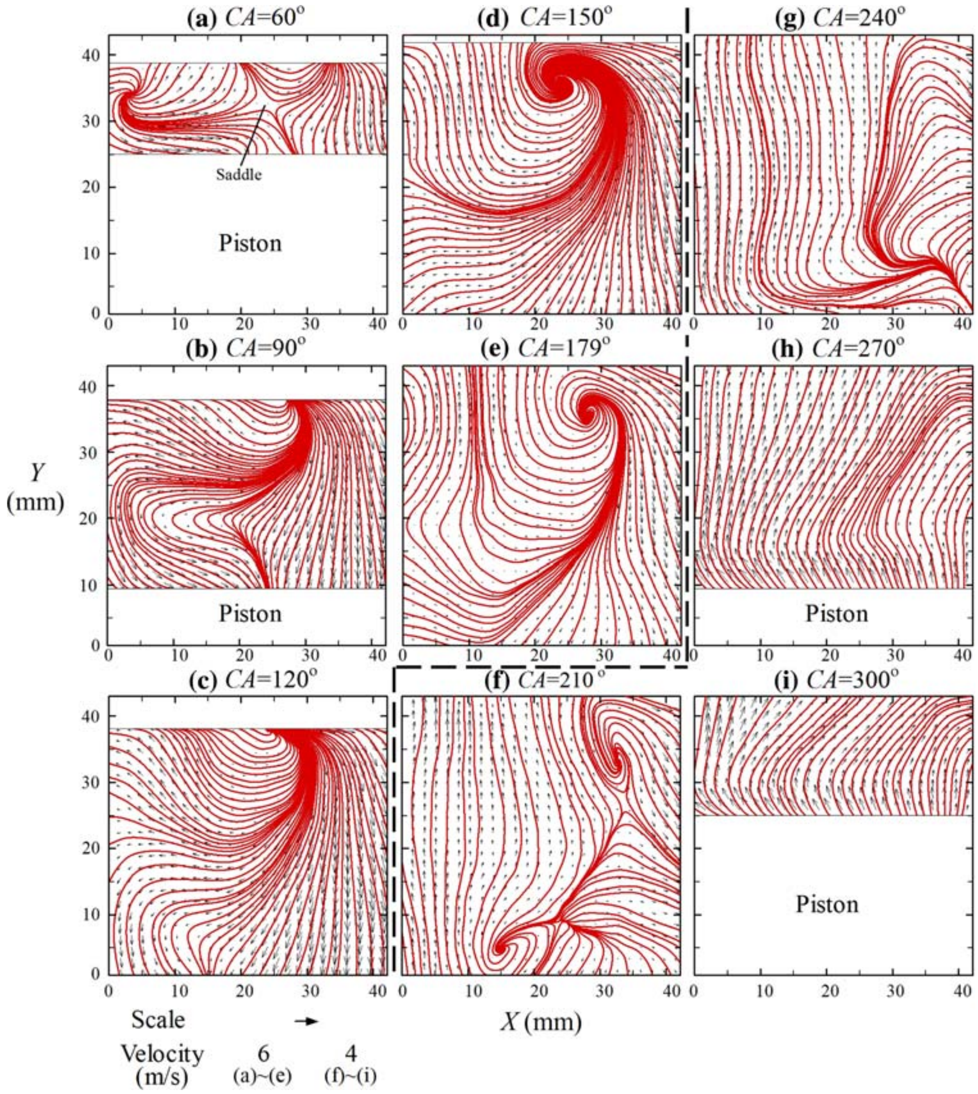

Figure 12a and b shows the instantaneous plane-averaged tumble ratios of the in-cylinder flows in the symmetry and offset planes, respectively. In the symmetry plane (Fig. 12a), the values of $T_{v,\mathrm{CA}}$ of the in-cylinder flow with the circular intake port generally decrease with the increase of the crank angle. During the intake stroke, $T_{v,\mathrm{CA}}$ decreases quickly with the increase of CA. During the compression stroke, the tumble ratio decreases to values lower than 0.15 because the flow patterns shown in Fig. 6 present no coherent, large-scale vortical flow structure. At CA = 300°, it attains negligibly small value of 0.06. The tumble ratio in the symmetry plane of the in-cylinder flow of the engine with elliptic intake port generally presents larger values than that with the circular intake port except at the beginning phase of the intake stroke. During the intake stroke, it increases with the increase of the crank angle to about 0.41 at CA = 120°, then decreases with the increase of crank angle to 0.17 at CA = 210°. During the mid- and final phases of the compression stroke, the tumble ratio unexpectedly increases to the level between 0.21 and 0.31 because large vortical flow structures appear during these phases (see Fig. 7). In the offset plane, as shown in Fig. 12b, the tumble ratios $T_{v,\mathrm{CA}}$ attain the highest values during the final phase of the intake stroke and decrease subsequently in the compression stroke. These variations correspond to the observations of flow patterns shown in Figs. 8 and 9. The values of the tumble ratio $T_{v,\mathrm{CA}}$ of the in-cylinder flow with the elliptic intake port are generally larger than those of the circular intake port. The difference is particularly significant during the intake stroke.

The cycle-averaged tumble ratio $\overline{T_v}$ can be obtained by taking the arithmetic average of the tumble ratios of Fig. 12a and b. The results are listed in Table 2. In the symmetry plane, the cycle-averaged tumble ratios are 0.187 and 0.301 for the cases of circular and elliptic intake ports, respectively. While in the offset plane, they are 0.261

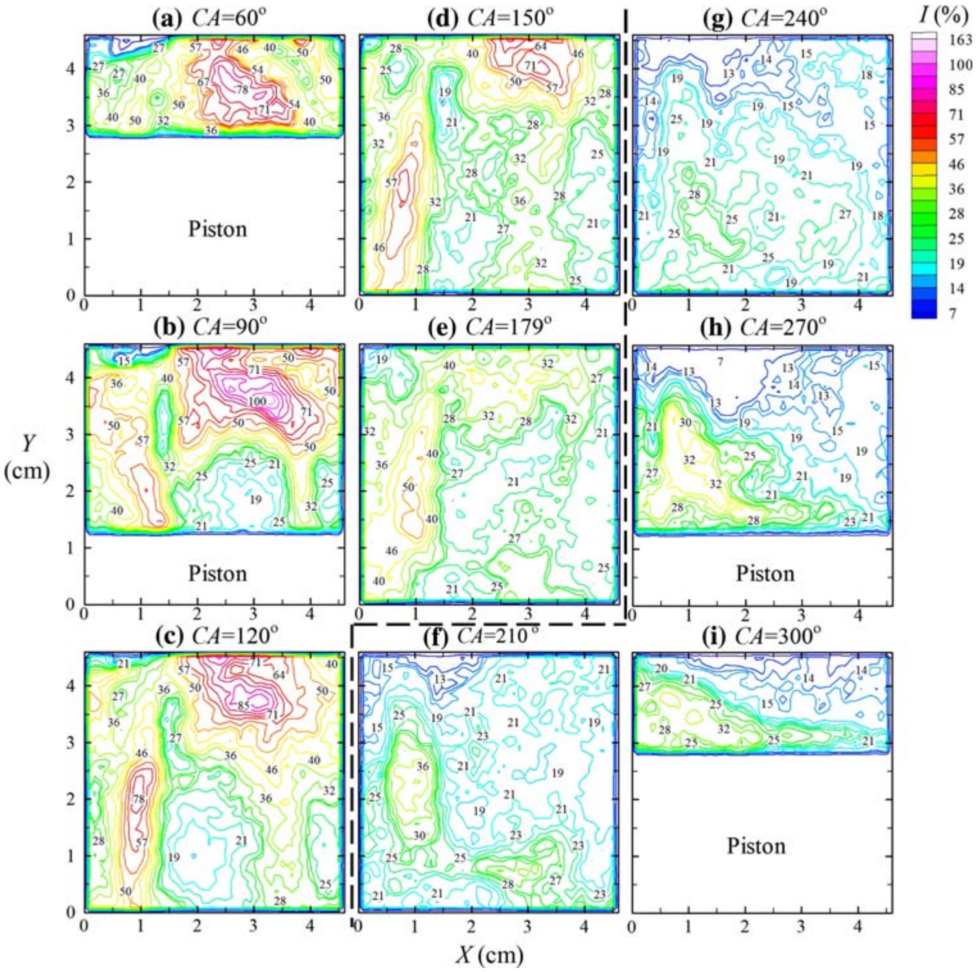

Fig. 10 Evolution of turbulence intensity distribution in symmetry plane during intake stroke (**a**–**e**) and compression stroke (**f**–**i**). Engine installed with circular intake port

and 0.358 for the cases of circular and elliptic intake ports, respectively. No matter whether it is the circular or the elliptic intake port, the cycle-averaged tumble ratios in the offset plane seem to be significantly larger than those in the symmetry plane. In the symmetry plane, the cycle-averaged tumble ratio of the engine with the elliptic port is larger than that with the circular port by 0.114 which increases drastically by 61%. In the offset plane, the difference is 0.097 which corresponds to about 37%.

3.3.2 *Turbulence intensities*

The plane-averaged turbulence intensities (I_{CA}) of the in-cylinder flows in the symmetry and offset planes at various crank angles are shown in Fig. 13a and b, respectively. In the symmetry plane (Fig. 13a), during the intake stroke the turbulence intensities of the in-cylinder flow for both cases of the circular and elliptic intake ports decrease with the increase of the crank angle. During the mid- and final stages of the compression stroke, they all increase very slightly with the increase of CA. The turbulence intensities of the in-cylinder flow of the engine with the elliptic intake port generally have larger values than those of the engine with the circular intake port. While in the offset plane, as shown in Fig. 13b, the differences are not so definite.

The cycle-averaged turbulence intensities $\bar{I}$ can be obtained by taking the arithmetic average of the instantaneous plane-averaged turbulence intensities of Fig. 13a and b. The results are listed in Table 2. In the symmetry plane, the cycle-averaged turbulence intensities are 0.293 and 0.332 for the cases with circular and elliptic intake ports, respectively. In the offset plane, they are 0.332 and 0.340 for the cases of circular and elliptic intake ports, respectively. In the symmetry plane, the cycle-averaged turbulence intensity of the engine with the elliptic intake port is increased by 0.039 which is an increase of 13% over that with the circular intake port. While in the offset plane, the difference between the two cases is comparatively insignificant.

3.4 Discussion

The measured volumetric efficiencies of the engines with the circular and elliptic intake ports (which are not shown

Fig. 11 Evolution of turbulence intensity distribution in symmetry plane during intake stroke (**a**–**e**) and compression stroke (**f**–**i**). Engine installed with elliptic intake port

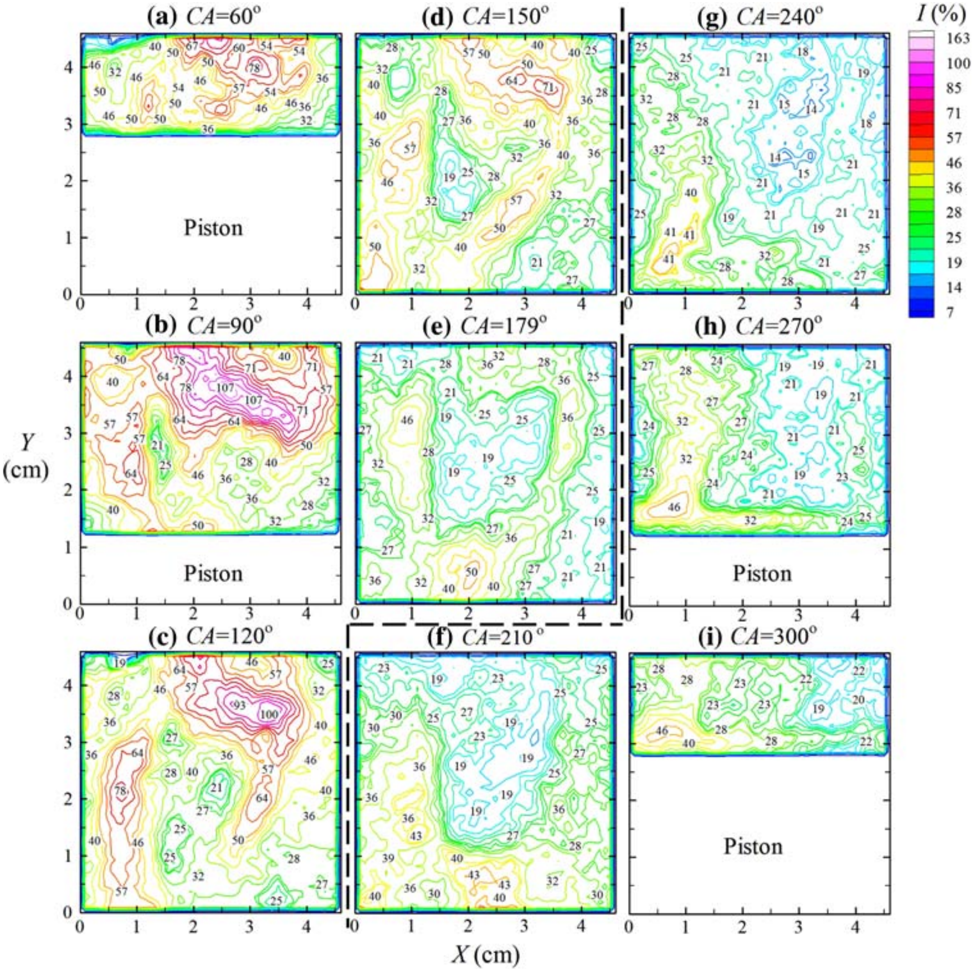

here) present only very negligible differences within 0–1%. This small difference would not cause significant differences of the engine performance. The measured torque (T), power output (P), specific fuel consumption (SFC), and exhaust hydro-carbon concentration (C_{HC}) of the engine at quarter throttle opening ($\alpha = 1/4$) are shown in Fig. 14a–d. The air/fuel ratios (A/F) at all engine speeds of Fig. 14 are fixed at about 13.5. It is obvious that the torque and power outputs of the engine with the elliptic intake port are appreciably larger than those of the engine with the circular port. However, the cases of the specific fuel consumption and the hydro-carbon emission are reversed. At low throttle opening ($\alpha = 1/4$), the fuel consumption and hydro-carbon exhaust may be notably reduced by using the elliptic intake port. At mid-throttle openings, say $\alpha = 1/2$ which is not shown here, this phenomenon still persists. At high-throttle openings, say $\alpha = 3/4$ and 1 (the case of $\alpha = 1$ is shown in Fig. 15), the engine performance presents similar behaviors, but the improvement caused by the elliptic intake port is not as significant as that at low-throttle openings except for the specific fuel consumption. The fuel consumption at wide-open throttle is still significantly decreased with the elliptic intake port. Because the PIV data were collected under the situation that the throttle valve is wide open, the engine performance data at wide-open throttle condition therefore are more relevant to the in-cylinder flow properties. As mentioned in the section of Introduction, the study of Stansfield et al. (2007) showed that the flow patterns of the in-cylinder flow would remain "similar" both at low and high engine speeds. However, at high engine speed the vortex sizes at corners of the engine cylinder would be enlarged and lead to higher tumble ratio. Their findings may explain that although the in-cylinder flow was diagnosed at $N = 2{,}000$ rpm in this study, the engine performances of the elliptic-port case still present similar improvement at higher engine speeds. At air/fuel ratios other than 13.5, the engine installed with the elliptic intake port also presents better torque, fuel consumption, and hydro-carbon emission, as shown in Fig. 16. It is obvious that the engine installed with the elliptic intake port can be operated at the stoichiometric condition or lean combustion range to reach the expectation of low fuel consumption and hydro-carbon emission and still maintain satisfactory power output.

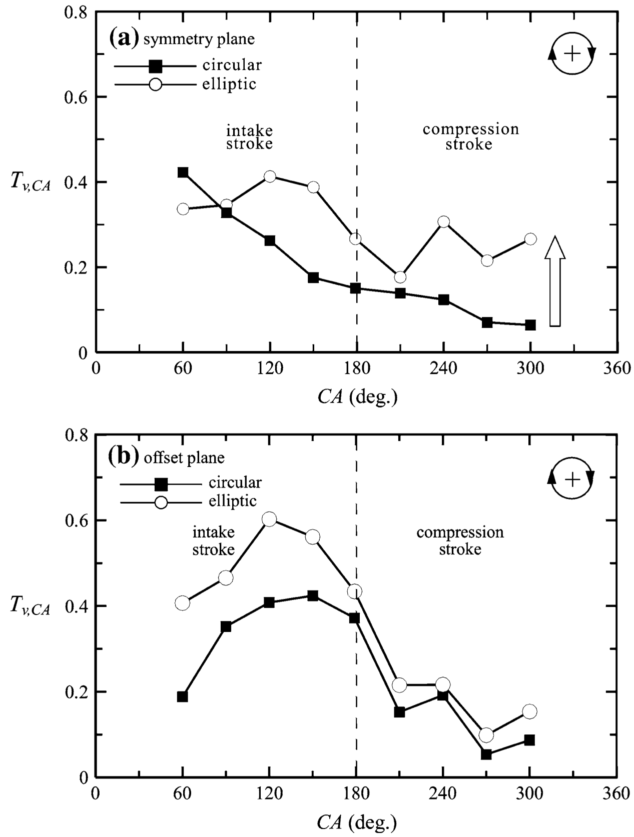

Fig. 12 Plane-averaged tumble ratio at various crank angles. **a** symmetry plane, **b** offset plane

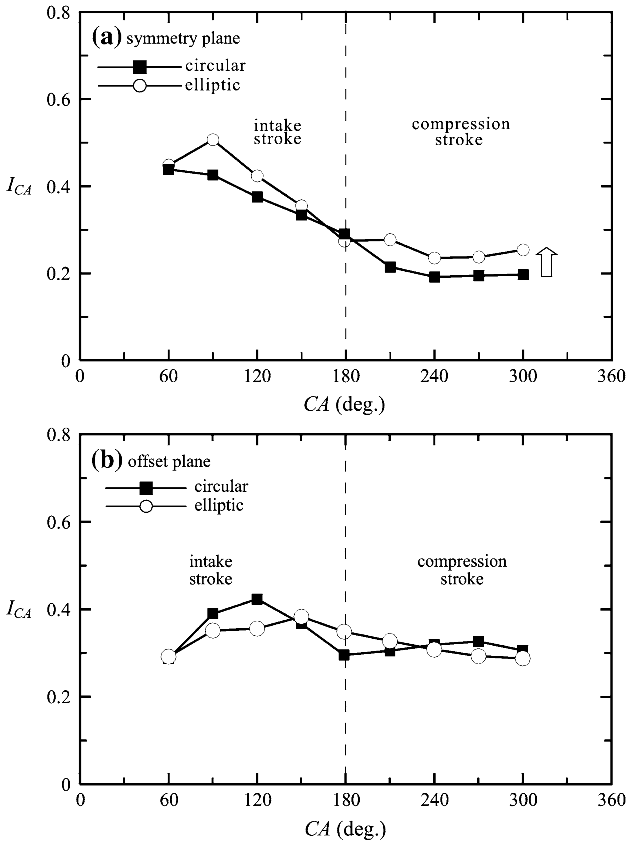

Fig. 13 Plane-averaged turbulence intensity at various crank angles. **a** symmetry plane, **b** offset plane

Table 2 Cycle-averaged tumble ratio ($\overline{T_v}$) and turbulence intensity ($\overline{I}$)

Cross section of intake port	Symmetry plane		Offset plane	
	$\overline{T_v}$	$\overline{I}$	$\overline{T_v}$	$\overline{I}$
Circular	0.187	0.293	0.261	0.332
Elliptic	0.301	0.332	0.358	0.340

Because the volumetric efficiencies of the engines installed with circular and elliptic intake ports are almost identical, the latter one would lead to a possibility of improvement in combustion by its flow characteristics. With the enhancement of combustion, the increase of the engine torque as well as the decrease of fuel consumption and hydrocarbon emission will come to dawn. The prominent increase in the tumble ratio corresponds to the increase of the vorticity. Physically, the vorticity is a quantitative estimate of the rotation rate. Its inverse counterpart, usually referred as circulation, can be interpreted as an index for the capability of diffusion of physical quantities (Tritton 1988). Higher vorticity implies a higher rotating rate, and smaller circulation implies a larger diffusivity for the physical quantities in the vortical flow. Besides, the enlarged turbulent fluctuations existing in the vortical flow would be beneficial to the transport of physical quantities (e.g., mixing) and could increase the turbulent flame speed (Tennekes and Lumley 1972). It is therefore argued that the flow properties induced by the featured flow characteristics in the cylinder of the engine installed with the elliptic intake port can be of significant contributions to the enhancement of the engine performance.

It is still unclear why the modification of in-let port configuration from circular to elliptic cross-section can lead to the increases of the tumble ratio and turbulence intensity. The elliptic port perhaps changes the flow distributions in the manifold and leads to the change of the boundary conditions before entering the cylinder. This subject may require further studies in the future.

4 Conclusions

The temporal/spatial evolution processes, tumble ratios, and turbulence intensities of the flows in the engine cylinder installed with the elliptic and circular intake ports are experimentally studied. It is found that during the intake

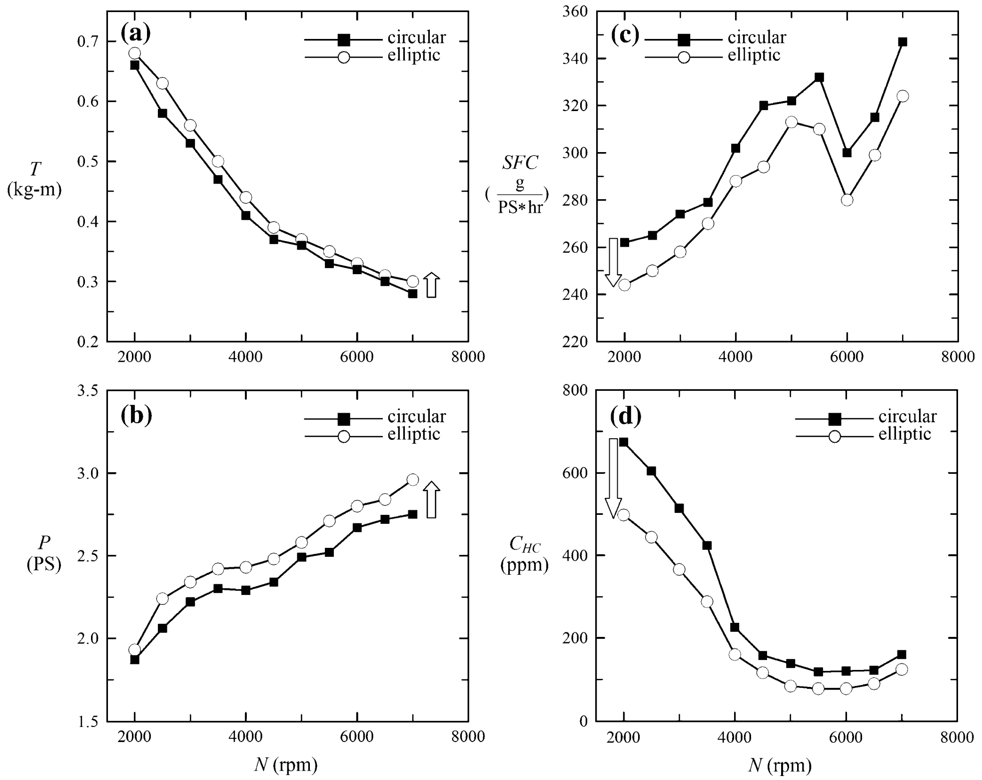

Fig. 14 Engine outputs at various engine speed. $\alpha = 1/4$, $A/F = 13.5$. **a** torque, **b** power, **c** specific fuel consumption, **d** concentration of hydrocarbon emission

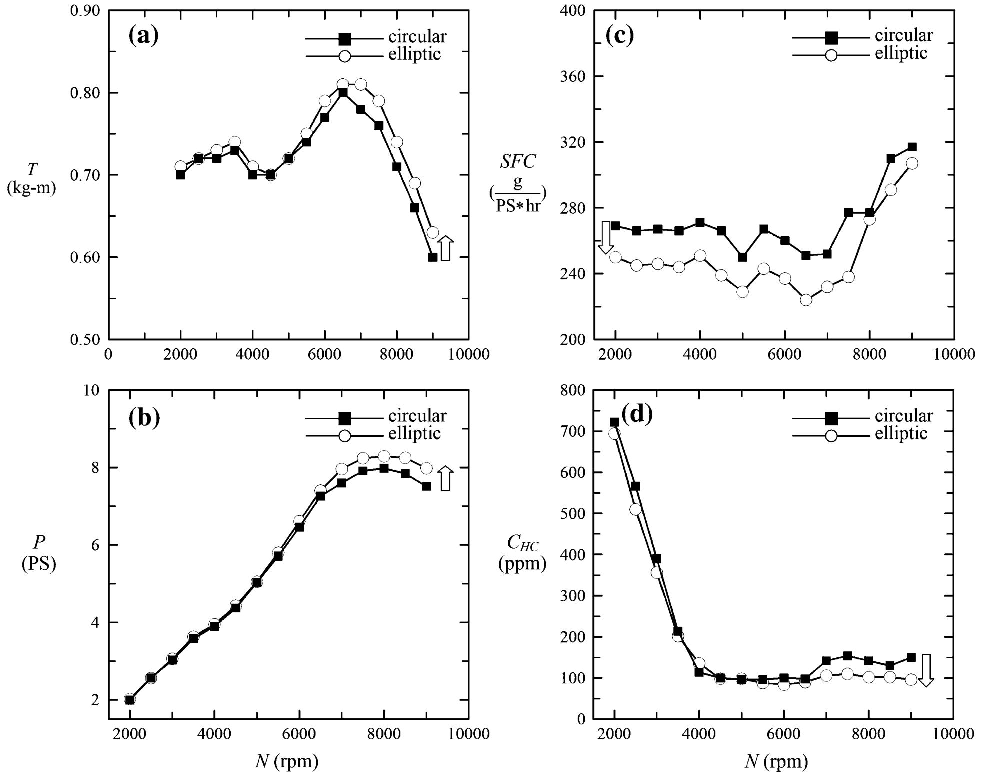

Fig. 15 Engine outputs at various engine speed. $\alpha = 1$, $A/F = 13.5$. **a** torque, **b** power, **c** specific fuel consumption, **d** concentration of hydrocarbon emission

stroke the elliptic intake port can initiate a vortex around the central region of the cylinder earlier than the circular intake port does. During the compression stroke, the central vortex created in the engine cylinder with the circular intake port disappears, while that in the engine cylinder with the elliptic intake port develops into the tumble

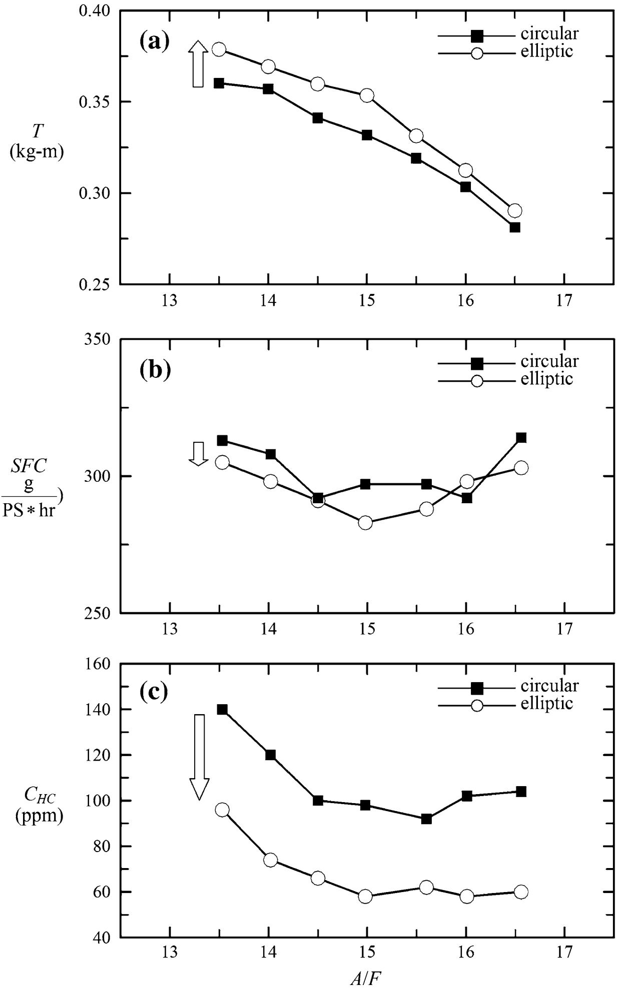

Fig. 16 Engine outputs at various air/fuel ratios. $\alpha = 1/4$, $N = 5{,}000$ rpm. **a** torque, **b** specific fuel consumption, **c** concentration of hydrocarbon emission

motion. Due to the featured vortical flow structure evolving in the cylinder, the cycle-averaged tumble ratio of the engine with the elliptic intake port is dramatically larger than that of the engine with the circular intake port. The cycle-averaged turbulence intensity in the symmetry plane of the engine with the elliptic intake port is larger than that of the engine with the circular intake port. Physically, larger tumble ratio and turbulence intensity imply larger rotation rate and diffusivity, and therefore could promote the mixing and flame propagation properties in the flow field. It is therefore argued that the combustion happened in the cylinder of the engine with the elliptic intake port would be intensified when compared with that of the engine with the circular intake port. The measured engine performances show close correlation with the flow characteristics: the torque and power output of the engine installed with the elliptic intake port are apparently larger than those of the engine with the circular intake port, while the specific fuel consumption and hydrocarbon exhaust of the engine with the elliptic intake port are drastically lower than those of the engine with the circular intake port.

References

Abernethy RB, Benedict RP, Doedell RB (1985) ASME measurement uncertainty. J Fluid Eng 107(1):161–164

Arcoumanis C, Godwin SN, Kim JW (1998) Effect of tumble strength on combustion and exhaust emissions in a single-cylinder, four-valve, spark-ignition engine, SAE paper 981044, Warrendale, PA

Calendini PO, Duverger T, Lecerf A, Trinite M (2000) In-cylinder velocity measurements with stereoscopic particle image velocimetry in a SI engine, SAE paper 2000-01-1798, Warrendale, PA

Ekchian A, Hoult DP (1979) Flow visualization study of the intake process of an internal combustion engine, SAE paper 790095, Warrendale, PA

Heywood JB (1987) Fluid motion within the cylinder of internal combustion engines. J Fluid Eng 109(1):3–35

Heywood JB (1988) Internal combustion engine fundamentals. McGraw-Hill, New York

Huang RF, Lin CL (1994) Visualized flow patterns of double concentric jets at low annulus velocities. AIAA J 32(9):1868–1874

Huang RF, Tsai FC (2001) Observation of swirling flows behind circular discs. AIAA J 39(6):1106–1112

Huang RF, Huang CW, Chang SB, Yang HS, Lin TW, Hsu WY (2005) Topological flow evolutions in cylinder of a motored engine during intake and compression strokes. J Fluids Struct 20(1):105–127

Hunt JCR, Abell CJ, Peterka JA, Woo H (1978) Kinematical studies of the flows around free or surface-mounted obstacles: applying topology to flow visualization. J Fluid Mech 86:299–446

Keane RD, Adrian RJ (1992) Theory of cross-correlation analysis of PIV images. Appl Sci Res 49(3):191–215

Khalighi B (1991) Study of the intake tumble motion by flow visualization and particle tracking velocimetry. Exp Fluid 10(4):230–236

Mei R (1996) Velocity fidelity of flow tracer particles. Exp Fluids 22(1):1–13

Rask RB (1979) Laser Doppler anemometer measurements in an internal combustion engine, SAE paper 790094, Warrendale, PA

Reeves M, Towers DP, Tavender B, Buckberry CH (1999) A high-speed all-digital techniques for cycle-resolved 2-D flow measurement and flow visualization within SI engine cylinders. Optics Lasers Eng 31(4):247–261

Stansfield P, Wigley G, Justham T, Catto J, Pitcher G (2007) PIV analysis of in-cylinder flow structures over a range of realistic engine speeds. Exp Fluids 43(1):135–146

Tennekes H, Lumley JL (1972) A first course in turbulence. MIT Press, Cambridge, pp 248–261

Tritton DJ (1988) Physical fluid dynamics. Oxford University Press, Oxford, pp 123–151

Yuan SW (1967) Foundations of fluid mechanics. Prentice-Hall, Englewood Cliffs, pp 202–204